Supporting Information

Fahrenbach et al. 10.1073/pnas.1109795108

SI Text

1. General Methods. All reagents were purchased from commercial suppliers (Aldrich or Fisher) and used without further purification. The compounds tris[(1-benzyl-1H-1,2,3-triazol-4-yl)methyl] amine (1) (TBTA) **S1** (2), **S2** (3), **CBPQT** • $4PF_6$ (4) and the catenane **C1** • $4PF_6$ (5) and **C2** • $4PF_6$ (6) were prepared according to literature procedures. Thin-layer chromatography was performed on silica gel 60 F254 (E. Merck). Column chromatography was carried out on silica gel 60F (Merck 9385, 0.040–0.063 mm). Both analytical and preparative high-pressure liquid chromatography (HPLC) were performed on reverse phase-HPLC (RP-HPLC) instruments, using C_{18} columns and a binary solvent system (MeCN and H_2O with 0.1% CF_3CO_2H). Nuclear magnetic resonance (NMR) spectra were recorded on a Bruker Avance 600 and Varian P-Inova 500 spectrometers, with working frequencies of 600 and 500 MHz for ^1H, and 150 and 125 MHz for ^{13}C nuclei, respectively. Chemical shifts are reported in ppm relative to the signals corresponding to the residual nondeuterated solvents (CD_3CN: δ1.94 ppm). High-resolution mass spectra were measured on a Finnigan LCQ iontrap mass spectrometer (HR-ESI). Cyclic voltammetry (CV) and chronocoulometry (CC) experiments were carried out at room temperature in argon-purged solutions of MeCN with a Gamry Multipurpose instrument (Reference 600) interfaced to a PC. All CV and CC experiments were performed using a glassy carbon working electrode (0.071 cm^2). The electrode surface was polished routinely with 0.05 μm alumina-water slurry on a felt surface immediately before use. The counter electrode was a Pt coil, and the reference electrode was a saturated calomel electrode unless otherwise noted. The concentration of the sample and supporting electrolyte tetrabutylammonium hexafluorophosphate (TBA • PF_6) were 1.0 mM and 0.1 M, respectively. The CV cell was dried in an oven immediately before use, and argon was continually flushed through the cell while it was cooled to room temperature to avoid condensation of water. Digital simulations of the CV experiments were performed using Digisim. The uncertainties in the ground-state distribution constants correspond to 3σ, where σ is standard deviation determined from least-squares fitting of the simulated data to the experimental data performed by the Digisim software. In the case of Eq. **5**, error analysis was based on a $\pm$10 mV uncertainty in measurement of E_{eq}.

2. Synthesis. **R** • $4PF_6$: The diazido-functionalized thread **S2** (500 mg, 0.69 mmol), the alkyne stopper **S1** (596 mg, 2.76 mmol), and **CBPQT** • $4PF_6$ (910 mg, 0.83 mmol) were dissolved in Me_2CO (100 mL). The solution was allowed to degas under argon for 30 min before adding $Cu(MeCN)_4PF_6$ (51 mg, 0.138 mmol) and TBTA (146 mg, 0.276 mmol) together as a solid. The reaction was allowed to stir for 1 d at room temperature under an inert atmosphere. A basic saturated solution of aqueous ethylenediaminetetraacetic acid was prepared using sodium bicarbonate and was added to the solution (20 mL), followed by H_2O (200 mL), and excess of NH_4PF_6 to induce precipitation of the crude product. The resulting green precipitate was collected by filtration and washed with H_2O (200 mL). The filtered solid was further purified using RP-HPLC. The pure fractions were concentrated to a minimal volume before adding a saturated aqueous solution of NH_4PF_6, filtering, and washing the green solid with H_2O to remove any excess of NH_4PF_6. We collected 550 mg (0.27 mmol, 39%) of a green solid, which was the target product **R** • $4PF_6$ in pure form. ^1H NMR (500 MHz, CD_3CN) δ = 8.93–8.80 (m, 6H), 8.71 (t, J = 7.2 Hz, 2H), 8.04–8.00 (m, 2H), 7.78–7.46 (m, 16H), 7.48–7.39 (m, 1H), 7.28–7.20 (m, 1H), 7.20–7.10 (m, 6H), 7.09–7.00 (m, 1H), 6.82 (d, J = 7.7 Hz, 1H), 6.78 (d, J = 7.5 Hz, 1H), 6.58 (d, J = 7.6 Hz, 1H), 6.19–5.95 (m, 2H), 5.70 (s, 4H), 5.51 (s, 4H), 4.86 (d, J = 8.4 Hz, 2H), 4.82 (s, 1H), 4.79 (s, 1H), 4.71–4.62 (m, 4H), 4.40–3.68 (m, 24H), 3.48–3.32 (m, 4H), 1.20 (s, 24H) ppm.^{13}C NMR (125 MHz, CD_3CN) δ = 153.6, 153.1, 152.4, 144.6, 144.5, 144.0, 143.6, 143.5, 143.4, 135.7, 135.1, 130.4, 130.3, 124.8, 124.7, 124.6, 123.9, 113.8, 113.7, 107.7, 107.5, 107.1, 105.6, 105.5, 105.3, 70.3, 70.0, 69.9, 69.7, 69.6, 69.2, 69.0, 68.8, 67.4, 67.3, 67.1, 67.0, 66.9, 66.7, 64.0, 53.8, 49.9, 49.5, 49.3, 29.6, 28.4, 26.0, 25.9, 23.3 ppm.

3. NMR Spectroscopy, Mass Spectrometry, and Analytical HPLC. **C1** • $4PF_6$: ^1H NMR (500 MHz, CD_3CN) δ = 8.94 (d, J = 6.4 Hz, 4H), 8.73 (d, J = 6.5 Hz, 4H), 7.75–7.30 (m, 20H), 6.73 (d, J = 7.4 Hz, 2H), 6.11 (s, 2H), 5.80–5.63 (m, 8H), 4.12 (s, 4H), 4.05–3.53 (m, 32H) ppm.

C2 • $4PF_6$: ^1H NMR (600 MHz, CD_3CN) δ = 9.18 (d, J = 6.0 Hz, 4H), 9.00 (d, J = 6.3 Hz, 4H), 7.90 (d, J = 6.3 Hz, 4H), 7.84 (d, J = 6.0 Hz, 4H), 7.69 (s, 8H), 6.25 (s, 2H), 5.80–5.60 (m, 8H), 4.18 (s, 4H), 3.91 (s, 4H), 3.86 (s, 8H), 3.81 (s, 4H), 3.75 (s, 4H), 3.58 (s, 4H), 3.31 (s, 4H) ppm.

4. Electrochemistry. Chronocoulometry experiments were performed on $\mathbf{R}^{4+}$, $\mathbf{C1}^{4+}$, and $\mathbf{C2}^{4+}$ in order to measure the diffusion coefficients of each species. In a typical run, the potential was stepped from 0 to +1 V, the response was measured, and then the potential was stepped back from +1 to 0 V, and again the response was recorded. The measured values of the slopes in the Cottrell plots in Fig. S4 *C–E* were used to calculate diffusion coefficients making use of the Anson equation, assuming in each step the number of electrons transferred was two, the surface area of the electrode was 0.071 cm^2, and the concentration was 1.0 mM. Uncertainties correspond to errors in the concentration of the sample, which was estimated to be $\pm$0.1 mM.

In order to test whether or not the switching between the two stations was concentration dependent, variable scan rate CV was performed on $\mathbf{R}^{4+}$ at concentrations of 1, 0.5, and 0.1 mM. The results of this study—shown in Fig. S5 *A–C*—reveal that the ground-state distribution relies very little on concentration, if at all, thus supporting the proposed intramolecular mechanism.

Using Ag/AgCl as a reference, a high scan rate CV (10 V/s) experiment was performed (Fig. S5*D*) on a 1 mM solution of $\mathbf{R}^{4+}$ in order to confirm the approximately 60 mV difference between E_{eq} and E_{MSCC}.

5. Digital Simulations. The ladder scheme shown in Fig. S6 was used to generate the simulated data shown in the main text, which was subsequently used to determine the ground-state distribution constant K for $\mathbf{R}^{4+}$, $\mathbf{C1}^{4+}$, and $\mathbf{C2}^{4+}$.

The following assumptions were made when producing the simulated CV traces shown in Fig. 4. Primarily, we assume that (*i*) the rate of electron transfer is always fast at each given scan rate, (*ii*), there is no background current arising from capacitance effects, and (*iii*) effects caused by diffusion on the amplitude of the current at slow scan rates are neglected. These assumptions are not far from the reality of the situation, when considering we are operating at slow scan rates so that (*i*) and (*ii*) hold firm. Our experimental data deviates from the ideality shown in Fig. 4*B* primarily in the case when the slowest scan rate of 10 $mV\,s^{-1}$ is employed, which is the limiting scan rate, such that assumption (*iii*) begins to be no longer true. The heterogeneous electron

transfer rate constants governing the transfer of electrons to and from the analyte in solution to the surface of the electrode can cause dramatic increases between anodic and cathodic peaks for a given reversible redox process especially at faster scan rates. In order to avoid these effects, we employed the polar solvent MeCN. In addition, the fact that we are using relatively slow scan rates further helps to ensure that these effects caused by slow heterogeneous electron transfer are not observed under our experimental conditions. The diffusion coefficients of the analytes also have an influence on current amplitude, which we have measured in order to arrive at a more accurate mechanistic picture. Effects caused by Ohmic resistance of the electrochemical cell can produce separation in the anodic and cathodic peaks of a redox couple at faster scan rates similar in fashion to that caused by slow heterogeneous electron transfer. We eliminate these effects by applying IR compensation whenever using scan rates greater than $1{,}000\ \mathrm{mV\,s^{-1}}$.

In order to avoid inducing convection of the solution as much as possible, particularly at slower scan rates, we performed all our experiments under a closed electrochemical cell. Specifically, before each scan was set to run, the cell was sealed off from the ambient atmosphere of the laboratory, cut off from the argon source, and allowed to rest such that convection caused by forces imposed upon by the flow of argon gas and ambient atmosphere at the boundary of the solution were minimized.

The following heterogenous electron transfer reactions were derived using the ladder scheme shown in Fig. S6.

Heterogeneous electron transfers.

$$\mathrm{MSCC^{2+} + e^- = MSCC^+} \qquad \mathrm{MSCC^+ + e^- = MSCC}$$
$$\mathrm{GSCC^{2+} + e^- = GSCC^+} \qquad \mathrm{GSCC^+ + e^- = GSCC}$$

The following homogenous chemical reactions were derived from the ladder scheme shown in Fig. S6. In order to generate the data shown in Fig. 4*B* of the main text, the ground-state distribution constant was varied, while in the slow scan rate regime. For the purposes of simulating the slow scan rate regime, a value of k_f (where $K = k_f/k_b$) was chosen as excessively large with respect to the scan rate. However, it is important to note that the k_f taking part in the ground-state distribution has been previously measured in some cases. For more details see ref. 7.

Homogeneous chemical reactions.

$$\mathrm{MSCC = GSCC} \qquad \mathrm{MSCC^+ = GSCC^+}$$
$$\mathrm{MSCC^{2+} = GSCC^{2+}}$$

In order to generate the data shown in Fig. 4*A* in the main text, the scan rate was systematically varied by factors of ten at given value of K and k_f, until such a point that increasing/decreasing the scan rate no longer affected the shape of the simulated CV.

Species parameters. Diffusion coefficients determined from chronocoulometry experiments for $\mathbf{R}^{4+}$, $\mathbf{C1}^{4+}$, and $\mathbf{C2}^{4+}$ were used when fitting the experimental data to the simulated data in order to determine the ground-state distribution constants. Diffusion coefficients for the MSCC and GSCC and their other $+1$ and $+2$ states were assumed to be the same. Diffusion coefficients for the $+1$ state was assumed to be the same as that for the $+2$ state.

Errors. First of all, consider that according to Eq. **5**, the distribution constant K depends exponentially on the difference in redox potentials, as measured in both the fast and slow scan rate regimes. It is important to observe that these values, derived from two independent methods of analysis, are consistent (Fig. S7) with each other on the logarithmic scale. Most likely, the differences in K produced from Eq. **5** and the fitting algorithm are a reflection of the deviation from the ideality that Eq. **5** represents and that which was determined from the more sophisticated model employed in the least-squares fitting.

1. Chan TR, Hilgraf R, Sharpless KB, Fokin VV (2004) Polytriazoles as copper(I)-stabilizing ligands in catalysis. *Org Lett* 6:2853–2855.
2. Aprahamian I, Olsen JC, Trabolsi A, Stoddart JF (2008) Tetrathiafulvalene radical cation dimerization in a bistable tripodal[4]rotaxane. *Chemistry* 14:3889–3895.
3. Aprahamian I, Dichtel WR, Ikeda T, Heath JR, Stoddart JF (2007) A clicked bistable[2] rotaxane. *Org Lett* 9:1287–1290.
4. Asakawa M, Brown CL, Pasini D, Stoddart JF, Wyatt PG (1996) Enantioselective recognition of amino acids by axially-chiral π-electron-deficient receptors. *J Org Chem* 61:7234–7235.
5. Asakawa M, et al. (1998) A chemically and electrochemically switchable [2]catenane incorporating a tetrathiafulvalene unit. *Angew Chem Int Ed Engl* 37:333–337.
6. Spruell JM, et al. (2009) A push-button molecular switch. *J Am Chem Soc.* 131:11571–11580.
7. Choi JW, et al. (2006) Ground state equilibrium thermodynamics and switching kinetics of a bistable [2]rotaxane switched in solution, polymer gels, and molecular electronic devices. *Chemistry* 12:261–279.

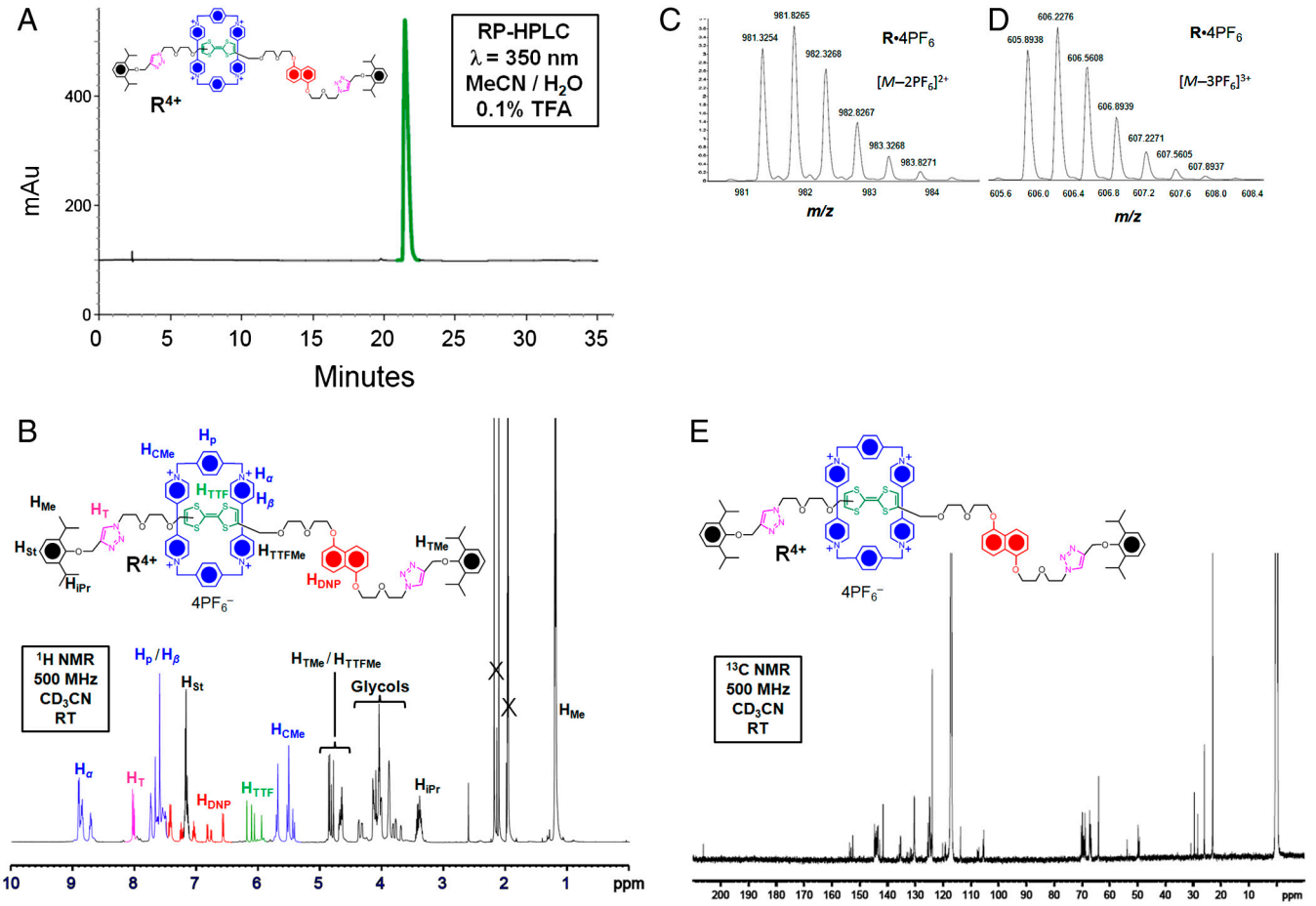

Fig. S1. (*A*) Analytical RP-HPLC trace of the [2]rotaxane **R** • $4PF_6$ and (*B*) annotated ^1H NMR spectrum. HR-ESI Mass spectrometry of the [2]rotaxane **R** • $4PF_6$ showing (*C*) the parent ion minus two PF_6^- counterions and (*D*) minus three PF_6^- counterions. (*E*) ^{13}C NMR spectrum of the [2]rotaxane **R** • $4PF_6$.

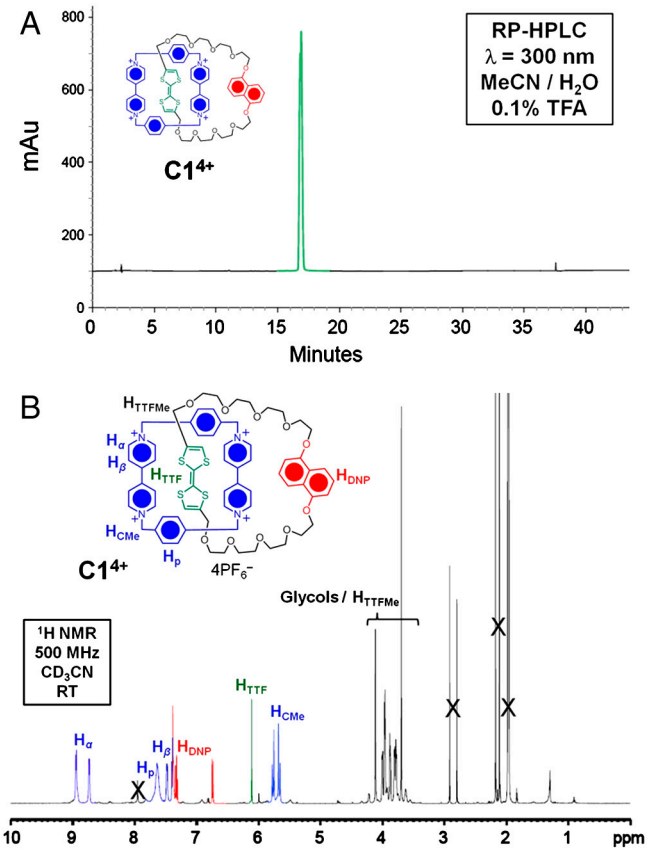

Fig. S2. (*A*) Analytical RP-HPLC trace of the [2]catenane **C1** • $4PF_6$ and (*B*) the annotated ^1H NMR spectrum.

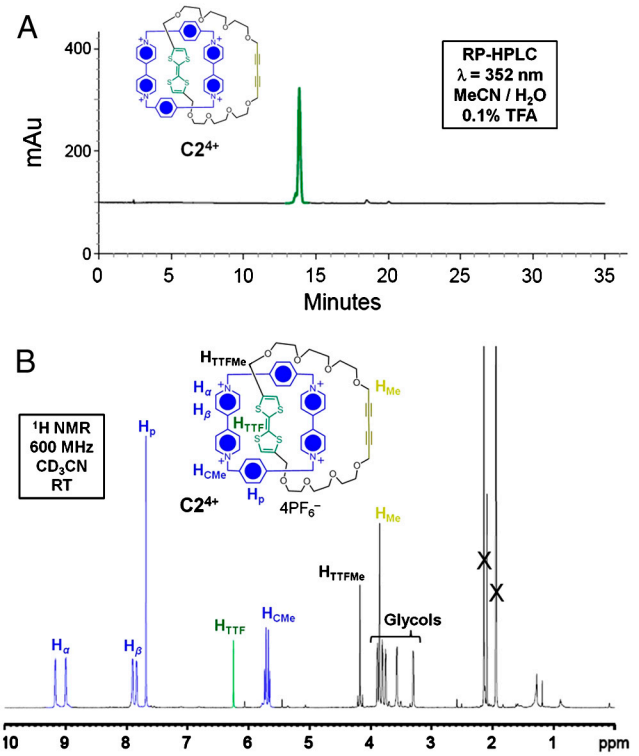

Fig. S3. (*A*) Analytical RP-HPLC trace of the [2]catenane **C2** • $4PF_6$ and (*B*) the annotated ^1H NMR spectrum.

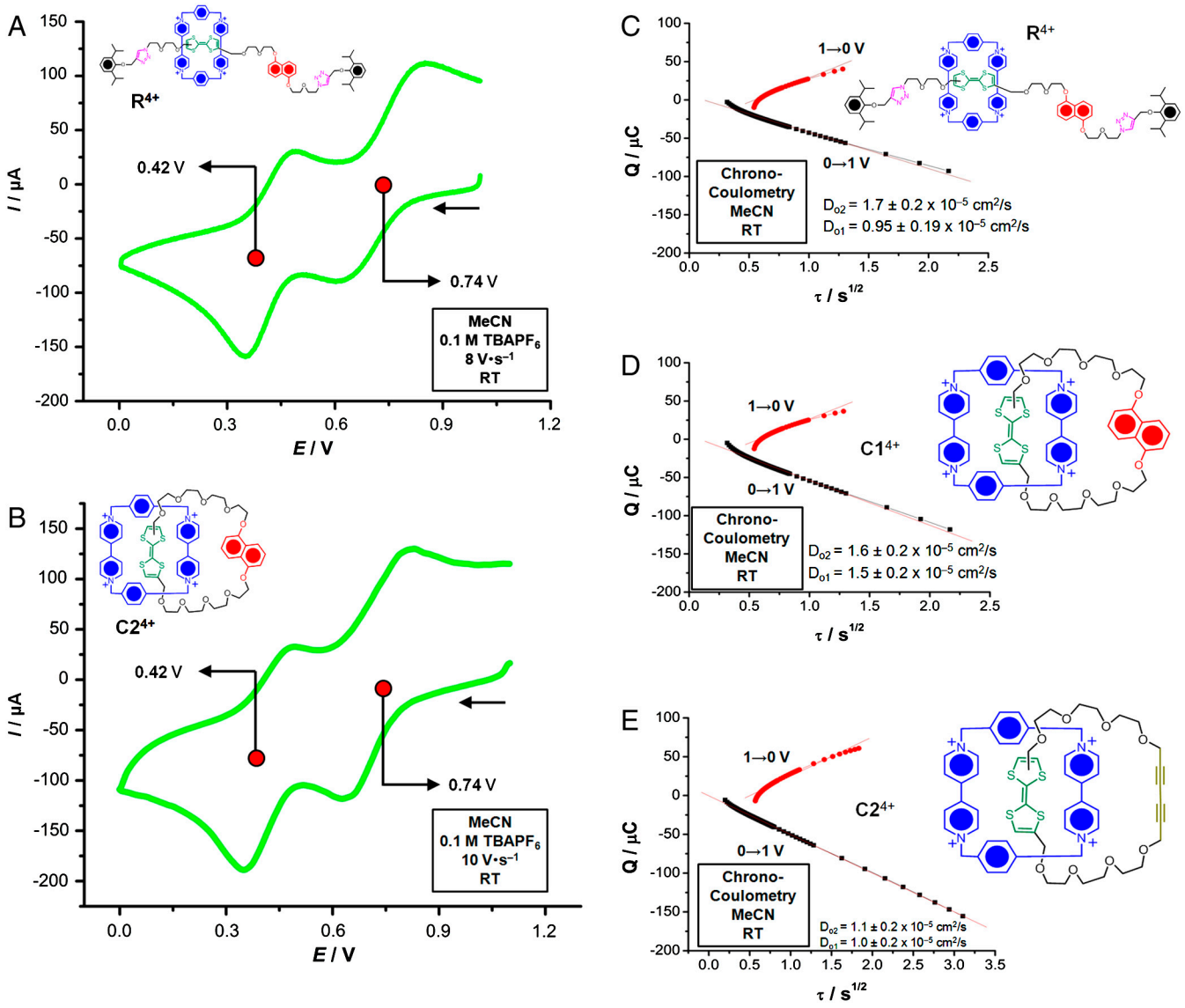

Fig. S4. (*A*) CV of the [2]rotaxane **R** • $4PF_6$ and (*B*) the catenane **C1** • $4PF_6$ taken in the fast scan rate regime. The redox potentials (E_{MSCC} and E_{MSCC+}) are depicted by the red dots. Each scan was background subtracted; IR compensation was applied. Integrated Cottrell plots of chronocoulometry data taken for (*C*) the rotaxane $\mathbf{R}^{4+}$, (*D*) the catenane $\mathbf{C1}^{4+}$, and (*E*) the catenane $\mathbf{C2}^{4+}$. D_{o1} corresponds to the step from 0 → 1 V, and D_{o2} corresponds to 1 → 0 V step.

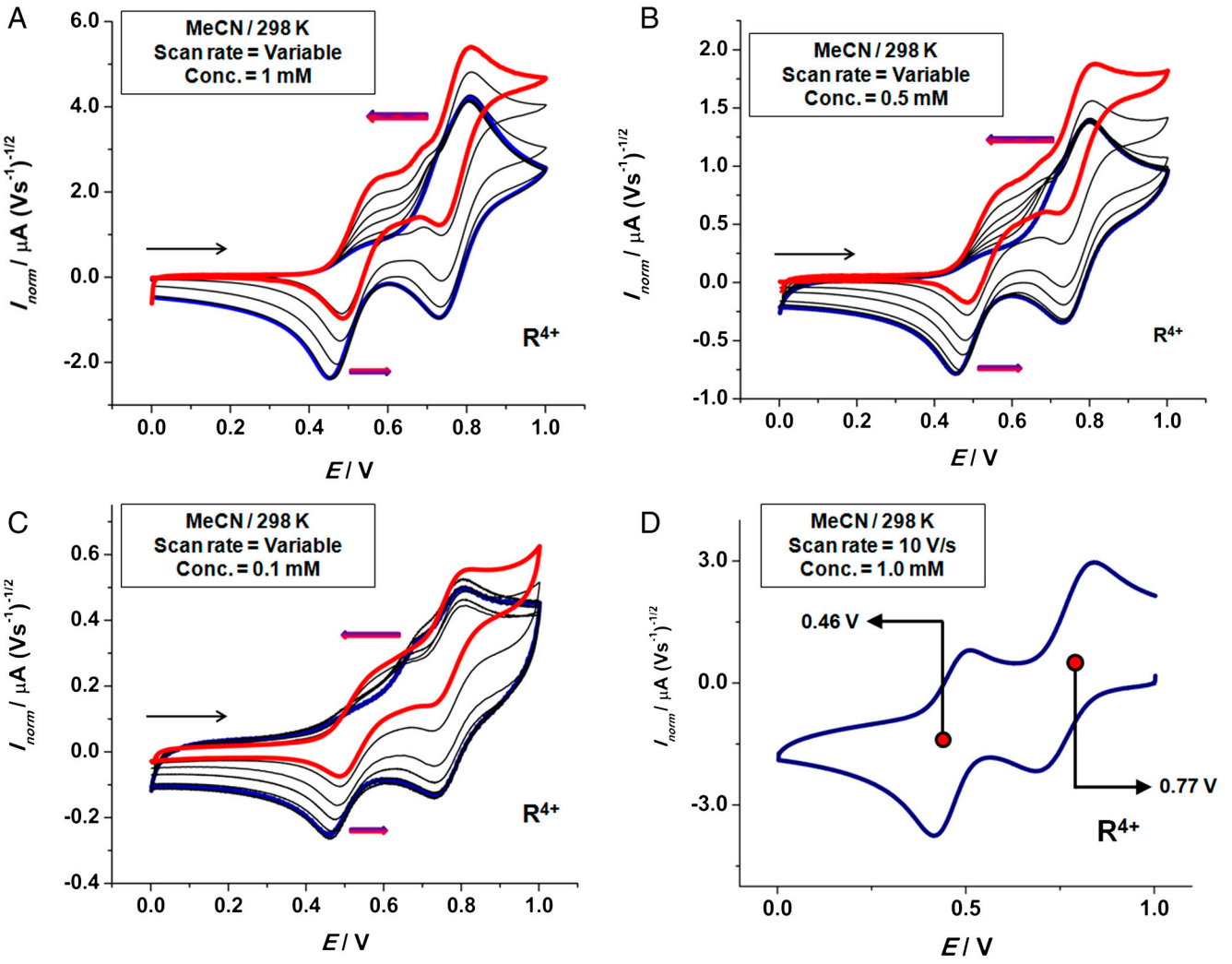

Fig. S5. Concentration study of $\mathbf{R}^{4+}$ using variable scan rate CV. The colored arrows represent the shifting of peaks. (*A*) A standard concentration of 1 mM was used followed by lower concentrations at (*B*) 0.5 mM and (*C*) 0.1 mM. Reference: Ag/AgCl. (*D*) CV of the [2]rotaxane $\mathbf{R}^{4+}$ at 10 V/s and 1 mM (Ag/AgCl reference).

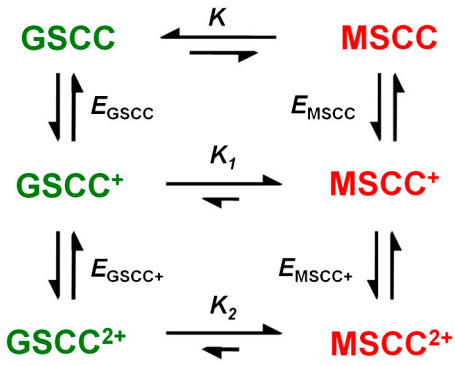

Fig. S6. Formal redox ladder scheme forming the basis for the general mechanism of bistable switching for the $\mathbf{R}^{4+}$, $\mathbf{C1}^{4+}$, and $\mathbf{C2}^{4+}$.

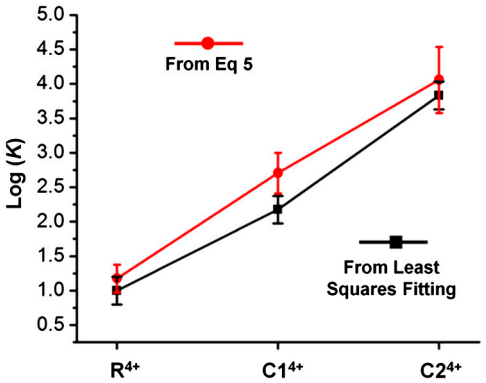

Fig. S7. A comparison of log(K) values and their associated errors for $\mathbf{R}^{4+}$, $\mathbf{C1}^{4+}$, and $\mathbf{C2}^{4+}$ determined by either using Eq. **5** or from X^2-fitting of the experimental data to the simulated scans.

Table S1. Heterogeneous electron transfer reactions, homogeneous chemical reactions, and CV parameters

	Reaction	E/V		
1	$MSCC^{2+} + e^- = MSCC^+$	0.74*		
2	$MSCC^+ + e^- = MSCC$	0.42*		
3	$GSCC^{2+} + e^- = GSCC^+$	1.25†		
4	$GSCC^+ + e^- = GSCC$	0.77‡		
	Reaction	K	k_f (s^{-1})	
5	$MSCC = GSCC$	variable	large	
6	$MSCC^+ = GSCC^+$	§	3.4×10^6 ¶	
7	$MSCC = GSCC^{2+}$	§	1.1×10^7 ¶	
E_{start}/V	E_{rev}/V	E_{end}/V	area/cm^2	v/V·s^{-1}
0	1.1	0	0.071	variable

*Values were determined from the data shown in Fig. S6.
†Value was based off of data reported in ref. 1.
‡Value estimated from measurements obtained on $\mathbf{R}^{4+}$ and $\mathbf{C1}^{4+}$ in the fast scan rate regime.
§Values were calculated automatically by the software.
¶Values were based upon theoretical data reported in ref. 2.

1 Flood AH, Nygaard S, Laursen BW, Jeppesen JO, Stoddart JF (2006) Locking down the electronic structure of (monopyrrolo)tetrathiafulvalene in [2]rotaxanes. *Org Lett* 8:2205–2208.
2 Kim H, et al. (2009) The free energy barrier of molecular motions in bistable [2]rotaxane molecular electronic devices. *J Phys Chem A* 113:2136–2143.

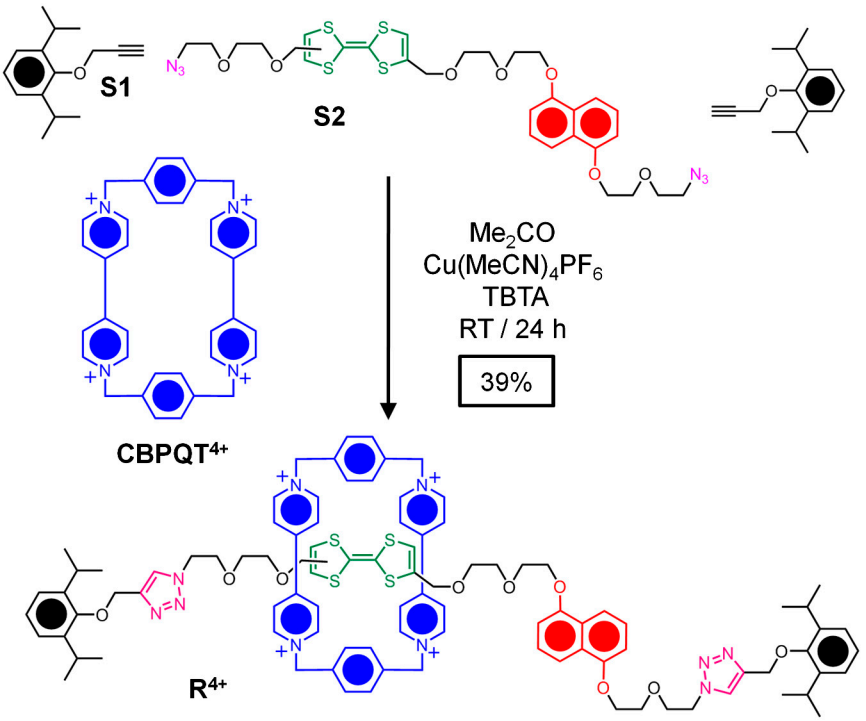

Scheme S1. Synthesis of the [2]rotaxane $\mathbf{R}^{4+}$.